

# Biomechanics-Based Curvature Estimation for Ultrasound-guided Flexible Needle Steering in Biological Tissues

PEDRO MOREIRA<sup>1</sup> and SARTHAK MISRA<sup>1,2</sup>

<sup>1</sup>Department of Biomechanical Engineering, MIRA Institute for Biomedical Technology and Technical Medicine, University of Twente, Horstring W-208, Drienerlolaan 5, 7522 NB Enschede, The Netherlands; and <sup>2</sup>Department of Biomedical Engineering, University of Groningen and University Medical Centre Groningen, Hanzeplein 1, 9700 RB Groningen, The Netherlands

(Received 15 July 2014; accepted 21 November 2014)

Associate Editor Xiaoxiang Zheng oversaw the review of this article.

**Abstract**—Needle-based procedures are commonly performed during minimally invasive surgery for treatment and diagnosis. Accurate needle tip placement is important for the success of the procedures. Misplacement of the needle tip might cause unsuccessful treatment or misdiagnosis. Robot-assisted needle insertion systems have been developed in order to steer flexible bevel-tipped needles. However, current systems depend on the information of maximum needle curvature, which is estimated by performing prior insertions. This work presents a new three-dimensional flexible needle steering system which integrates an optimal steering control, ultrasound-based needle tracking system, needle deflection model, online needle curvature estimation and offline curvature estimation based on biomechanics properties. The online and the offline curvature estimations are used to update the steering control in real time. The system is evaluated by experiments in gelatin phantoms and biological tissues (chicken breast tissues). The average targeting error in gelatin phantoms is  $0.42 \pm 0.17$  mm, and in biological tissues is  $1.63 \pm 0.29$  mm. The system is able to accurately steer a flexible needle in multi-layer phantoms and biological tissues without performing prior insertions to estimate the maximum needle curvature.

**Keywords**—Minimally invasive surgery, Needle steering, Needle-tissue interaction model, Flexible needle deflection, Needle curvature estimation.

## INTRODUCTION

Conventional open surgeries are being replaced by minimally invasive surgeries in order to reduce patient trauma and the overall costs.<sup>30</sup> Among the existing min-

imally invasive surgical techniques, needle-based procedures appear as the most common clinical intervention.<sup>3</sup> Needle-based procedures are used for treatment and diagnosis purposes, such as biopsy, brachytherapy, ablation, and neurosurgery.<sup>23</sup> The success rate of these interventions depends on the needle tip placement accuracy. Misdiagnosis or unsuccessful treatment might occur due to misplacement of the needle tip. Needle deflection, unexpected tissue deformation and difficulty accessing targets due to anatomical obstacles are common factors that affect the targeting accuracy. Currently, most of the needles used in percutaneous procedures are relatively stiff, and have an asymmetric tip to cut and penetrate the tissue. However, those needles may cause tissue damage and have limited steerability.

The use of thin and flexible needles can reduce the undesired tissue deformation and increase needle steerability. Bevel-tipped flexible needles naturally bend when they are inserted through the tissue. The enhanced steerability of flexible needles allows the clinician to maneuver around obstacles towards areas that are unreachable by rigid needles. Several clinical applications can benefit from the use of flexible needles such as delivery of systemic agents into the brain, ablation in the liver, transperineal prostate biopsy and many other possibilities. However, it is challenging to manually steer flexible needles. Robotic systems have been developed to assist clinicians in steering flexible needles towards a desired target.<sup>8</sup> These systems require a steering control algorithm, a needle tip tracking system and an accurate needle deflection model. Kinematic models for flexible needles with asymmetric tip have been developed assuming that the needle follows a circular path. These models have the maximum needle curvature as a model parameter. In current methods for flexible needle steering, the maximum curvature is determined by

Address correspondence to Pedro Moreira, Department of Biomechanical Engineering, MIRA Institute for Biomedical Technology and Technical Medicine, University of Twente, Horstring W-208, Drienerlolaan 5, 7522 NB Enschede, The Netherlands. Electronic mail: p.lopesdaftomoreira@utwente.nl

pre-operative needle insertions. However, performing additional needle insertions to estimate the maximum curvature contradicts the idea of minimally invasive surgery. Additionally, those models consider the tissue as a homogeneous environment, but biological tissues are usually inhomogeneous. Therefore, it is important to design a steering method capable of performing accurate needle tip placement in inhomogeneous tissues. The method should be able to accurately estimate the needle curvature using online needle tracking information and patient-specific biomechanics-based needle-tissue interaction model.

### Related Work

Robot-assisted needle insertion has been an active research topic in the last decade.<sup>8</sup> Needle steering methods using base motions outside the tissue to guide the needle towards a target were presented by DiMaio and Salcudean,<sup>9</sup> and Glozman and Shoham.<sup>14</sup> The type of needles used in these experiments and the base manipulation may produce tissue damage and target motion. This target motion can lead to needle tip misplacement. In order to cope with tissue damage and deformation, several research groups have been studying the use of thin and flexible needles. Thin and flexible steerable needles induce less target motion and their steerability is higher than conventional needles.<sup>1</sup> Bevel-tipped flexible needles naturally bend when they are inserted through the tissue and can be steered by rotating their base along the insertion axis during the insertion.

It is of major importance to understand how the needle deflects in order to steer a bevel-tipped flexible needle. A kinematic model for bevel-tipped flexible needles based on the nonholonomic unicycle model was developed by Webster *et al.*<sup>29</sup> The model predicts the needle deflection assuming that the needle always follows a circular path with constant curvature. The kinematic model proposed by Webster *et al.* was modified by Minhas *et al.*<sup>16</sup> in order to achieve paths with different curvatures. A steering system using the duty cycling technique that was first proposed by Engh *et al.*<sup>11</sup> The duty cycling technique is based on the idea of inserting and rotating the needle simultaneously providing different needle curvatures during the insertion. Flexible needle steering using duty-cycled rotations have been used in two dimensional<sup>6</sup> (2D) and three dimensional<sup>22</sup> (3D) insertions. Recently, Abayazid *et al.* have proposed a flexible needle steering based on a kinematic deflection model using US images to track the needle in real time.<sup>1</sup> A similar algorithm was implemented in 3D using a US-based needle tracking systems.<sup>2</sup> All these kinematic models and steering methods are based on the assumption that the maximum needle curvature is known. In these previous works, the maximum curvatures were

estimated by prior insertions, which is undesirable in minimally invasive surgery. Additionally, the models also consider a constant curvature throughout the insertion. Unfortunately, in biological tissues constant curvatures are unlikely. The experimental results presented by Robert *et al.*<sup>24</sup> show that the deflections of needles inserted into soft tissues are not constant during the insertion. Sadjadi *et al.*<sup>26</sup> presented a simulation study of combining electromagnetic trackers and needle deflection model using Kalman filtering techniques to estimate the needle curvature. An online curvature estimation of flexible needles inserted into biological soft tissues was proposed by Moreira *et al.*<sup>19</sup> However, only the presented online curvature estimation may not be the best solution if the needle undergoes a straight path. In these cases, the solution of the curvature fitting might not be guaranteed due to the low rank of the data matrix used in the least square problem. A more robust estimation can be achieved merging online estimation and biomechanics-based needle-tissue model.

Biomechanics-based needle-tissue models can also be used to determine the needle tip motion during an insertion procedure. Misra *et al.*<sup>18</sup> proposed a mechanics-based model to predict needle tip motion in planar insertions. Later, Roesthuis *et al.*<sup>25</sup> extended the model to predict 3D needle deflections. The model incorporates the needle tip force, distributed load and elastic foundation stiffness, which were also estimated during prior insertions. The deflection model proposed by Asadian *et al.*<sup>5</sup> estimates the amount of needle deflection by combining the beam theory with virtual springs used to represent the tissue resistance. Moreover, several works based on finite element (FE) methods have been presented. DiMaio and Salcudean<sup>9</sup> presented a FE model to simulate insertions of rigid needles. Chun *et al.*<sup>7</sup> presented a study of needle-tissue interaction forces on breast tissues and compared the experimental results to FE simulations. Although accurate, the computational time required for FE-based models limits the use of such models in real time needle insertion systems. Analytical models have also been proposed to determine needle-tissue interaction forces.<sup>17</sup> These interaction forces can be used to predict and estimate the needle curvature during the insertion.<sup>4</sup>

An experimental study to evaluate the interaction forces and needle curvature in *in vivo* and *ex vivo* tissues was presented by Majewicz *et al.*<sup>15</sup> The results show that the needle deflection is more pronounced in *ex vivo* tissues than in *in vivo* tissues due to their increased stiffness. Although several works about needle-tissue interaction have been presented,<sup>17</sup> the direct relationship between tissue properties and needle curvature has not been presented. This work proposes a novel steering algorithm that merges online curvature

estimation and the relationship between tissue's Young's modulus and needle curvature.

### Contributions

This paper presents a novel three-dimensional (3D) flexible needle steering system which integrates an optimal steering control, ultrasound (US)-based needle tracking system, needle deflection model, online needle curvature estimation and offline curvature estimation based on biomechanics needle-tissue model. The goal of this work is to demonstrate the feasibility of combining the optimal steering control, the online and the offline curvature estimation to increase the insertion accuracy. In order to avoid invasive pre-operative procedures, such as performing prior needle insertions to estimate the maximum curvature before each steering experiment, the biomechanics-based model relates the tissue's Young's modulus to the maximum needle curvature. The Young's modulus is estimated by using acoustic radiation force impulse (ARFI) imaging technique, which is a non-invasive method. The needle curvature information provided by the offline estimation is fused with an online curvature estimation. The main contributions of this paper are: (1) a relationship between tissue Young's modulus and needle curvature using a non-invasive method to define the needle curvature. (2) Combination of online and offline needle curvature estimation. (3) Steering algorithm using the estimated curvature to define the best needle rotation that minimizes the targeting error. Experiments steering a flexible needle toward a real target on two-layer gelatin phantom and biological tissues are presented in order to validate the proposed method (Fig. 1). Experiments with virtual moving targets are also presented to evaluate the targeting accuracy in the presence of physiological motions.

## MATERIALS AND METHODS

This section describes the biomechanics model and the offline estimation provided by the relationship between Young's modulus and needle curvature. The kinematic deflection model, the needle steering control and the online curvature estimation are also presented.

### Biomechanics Model and Offline Curvature Estimation

A bevel-tipped flexible needle deflects when inserted in a tissue due to the interaction between the bevel tip and the tissue. Several aspects influence the magnitude of needle deflection, such as insertion velocity, needle material, bevel angle, needle diameter, and tissue properties. The needle properties and the insertion velocity are defined prior to the insertion procedure and can be chosen

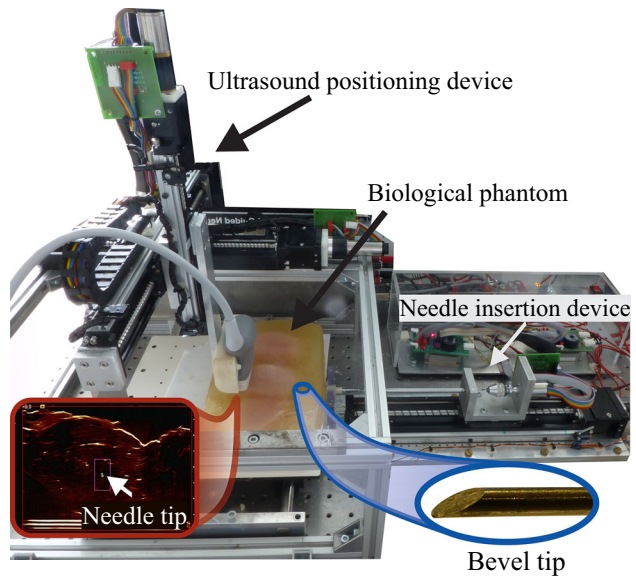


**FIGURE 1.** A robotic device inserts and axially rotates a bevel-tipped flexible needle into a phantom composed by gelatin and *in vitro* biological tissues (chicken breast). The needle is steered towards a real target while avoiding a real obstacle. An ultrasound-based needle tracker estimates the needle tip pose.

by the clinician according to the type of procedure.<sup>27</sup> On the other hand, tissue properties vary depending on the organs traversed by the needle during the insertion, and cannot be controlled by the clinician.

Previous work suggests that the needle deflection is closely dependent on the elasticity of the tissue. This section presents a relationship between the tissue elasticity (Young's modulus) and the needle curvature. The Young's modulus of tissues is estimated by a noninvasive method known as ARFI imaging technique.

### Young's Modulus Estimation

The Young's modulus of the phantoms are estimated using a commercially available implementation of an US-based ARFI imaging technique, known as Virtual Touch™ Quantification, available on the Siemens Acuson S2000 US machine (Siemens AG, Erlangen, Germany). The technique measures the shear wave velocity, which is used to calculate the Young's modulus of the phantom. The shear wave velocity ( $c_T$ ) is related to the shear modulus ( $G$ ) and density ( $\rho$ ) by<sup>20</sup>

$$c_T = \sqrt{\frac{G}{\rho}} \quad (1)$$

The Young's modulus ( $E$ ) is given by

$$E = 2G(1 + \mu) \quad (2)$$

where  $\mu$  is the Poisson's ratio. The gelatin phantoms are considered as almost incompressible materials, i.e.,

the Poisson's ratio is assumed to be 0.49 for all phantoms.<sup>12</sup> Using Eq. (1) in (2), the Young's modulus is calculated as

$$E = 2\rho c_T^2(1 + \mu) \quad (3)$$

The shear wave is measured in ten different locations of each phantom and the average of these values are used to calculate the Young's modulus.

#### Needle Curvature Estimation

The relationship between the Young's modulus of the tissue and the needle curvature is defined by performing a series of insertions in gelatin phantoms with known Young's modulus. The database acquired in these experiments is used to define the relationship between the needle curvature and Young's modulus. It is important to notice that this analysis is performed once. Then, this relationship is used to define the needle curvature before each steering experiment presented in "Results" section. The Young's modulus of the phantoms is varied by changing the gelatin concentration. The insertions are performed using the insertion device presented in Fig. 1. The needle is a Nitinol wire ( $E = 75$  GPa) with a diameter of 0.5 mm and bevel angle of 30°. The needle insertion is performed without any axial rotation and the tip position is estimated by the US-based tracking system presented in "Ultrasound-based needle tracking and offline path planning" section. The needle curvature is estimated by fitting a circle to the set of 3D needle tip positions. Ten 50 mm insertions are performed on six phantoms with different Young's modulus. The needle curvature information is then related to the Young's modulus of each phantom.

#### Needle Curvature Vs. Young's Modulus

The radius of curvature estimated for each phantom and the Young's modulus of the phantom is used to find the function that relates the Young's modulus and the radius of curvature. The relationship is defined by fitting a power function to the experimental data. The experimental results and the fitted function are plotted in Fig. 2. The radius of curvature is then given by

$$r = 17900E^{-0.49} + 25.98 \quad (4)$$

where  $r$  is the radius of curvature and  $E$  is the Young's modulus. The fitted function (4) is then used to perform the offline curvature estimation based on the Young's modulus information that can be pre-operatively estimated using the ARFI imaging technique. The function given by Eq. (4) is valid for the characteristics of the needle used in this work. However, the technique presented in this section can be replicated to define the relationship between Young's modulus and needle deflection with other needle properties. The needle steering control uses (4) to improve the robustness and accuracy of the curvature estimation.

#### Needle Steering Control

In this subsection the method used in the steering control is presented. First, the US-based tracking is presented followed by the needle deflection model, the optimal steering algorithm and the online curvature estimation.

#### Ultrasound-Based Needle Tracking and Offline Path Planning

The 3D needle tip pose (position and orientation) is estimated using a 2D US transducer. The transducer is

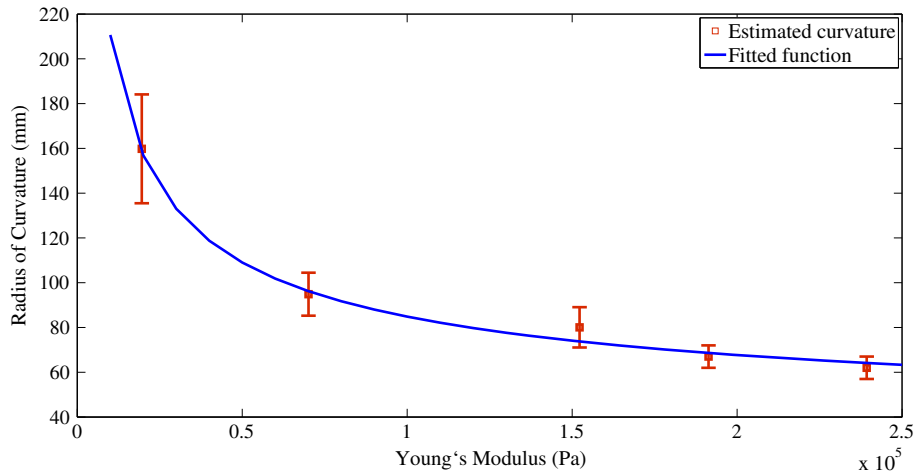


FIGURE 2. Radius of curvature vs. Young's modulus. The red dots are the experimental results of curvature estimation and its standard deviation defined by 10 insertions at each Young's modulus value. The blue line is the fitted function given by  $r = 17900E^{-0.49} + 25.98$ , where  $r$  is the radius of curvature and  $E$  is the Young's modulus of the phantom.

placed perpendicular to the needle to measure the tip position.<sup>28</sup> During the needle insertion, the transducer is repositioned to track the needle tip. The transducer is driven by a robotic device, that uses the insertion velocity corrected by tip velocities to determine out-of-plane motion. An image processing algorithm is used to estimate the needle tip position from the US image applying basic image processing techniques such as, median filtering, thresholding, erosion, and dilation. Using the information about the transducer location provided by the robotic device and the location of the needle tip on the US image, it is possible to determine the 3D needle tip pose.<sup>28</sup> The needle tracking runs in a frequency of 25 Hz and the maximum mean errors in the estimated needle tip positions are 0.64, 0.25, and 0.27 mm along the  $x$ -,  $y$ -, and  $z$ -axes, respectively.

The US tracking system is also used to scan the phantom before each experiment in order to define the obstacle and target locations. The desired needle path is then computed offline using the obstacle and target location. The path is calculated by an algorithm that uses splines to find a path that goes from the insertion point to

the target location, while avoiding the obstacle. The path is composed by a sequence of points with a 1.2 mm interval, that is used by the optimal steering algorithm.

#### Needle Tip Prediction Model

The needle deflection model predicts the needle tip position based on the needle rotation and insertion. The predicted needle tip position  $\hat{p}_{tip}^0(k+1)$  in the reference frame ( $\mathcal{H}_0$ ) is the sum of the current tip position  $\hat{p}_{tip}^0(k)$  plus an incremental 3D tip motion (Fig. 3), where  $k$  is the discrete index. This incremental motion is a result of the needle insertion and deflection. The incremental motion with respect to the needle tip frame depends on the insertion velocity ( $v_{ins}$ ) and the radius of needle curvature  $r(k)$ . Assuming that this motion is a circular path,<sup>29</sup> the 3D incremental tip motion is defined as

$$r(k)^2 = (x_{inc}(k) - a)^2 + (y_{inc}(k) - b)^2 + (z_{inc}(k) - c)^2 \quad (5)$$

where  $(a, b, c)$  is the center of the circular motion,  $r(k)$  is the radius and  $x_{inc}(k)$ ,  $y_{inc}(k)$ , and  $z_{inc}(k)$  are the

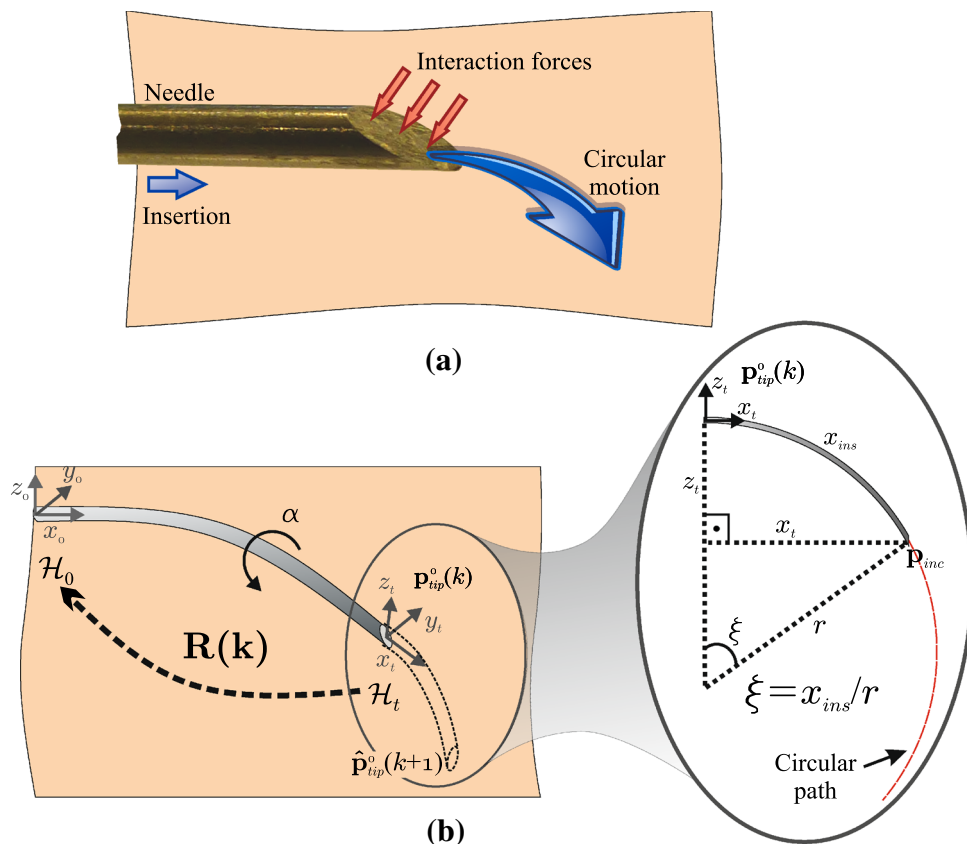


**FIGURE 3.** Needle deflection. (a) The bevel-tipped flexible needle bends in a circular motion due to the interaction forces between the bevel tip and the tissue. (b) The needle deflection model predicts the needle tip position ( $\hat{p}_{tip}^0(k+1)$ ) by calculating the incremental tip motion and using the rotation matrix ( $R(k)$ ) from the needle tip frame ( $\mathcal{H}_t$ ) to the initial reference frame ( $\mathcal{H}_0$ ). The needle axial rotation ( $\alpha(k)$ ) is an input for the needle deflection model. The components of the incremental tip motion ( $x_{inc}(k)$ ,  $y_{inc}(k)$ ,  $z_{inc}(k)$ ) are calculated by a trigonometric relation between the insertion step length ( $x_{ins}$ ), the radius of the circular motion ( $r$ ) and the angle ( $\xi$ ).

components of the incremental tip motion. This incremental motion, in the tip coordinate frame ( $\mathcal{H}_t$ ), is always an arc in the  $x_t$ -plane since the needle bends in the direction of the bevel tip orientation (Fig. 3a) if it is not rotated. The center of the circular incremental motion in the tip coordinate frame ( $\mathcal{H}_t$ ) is  $(a, b, c) = (0, 0, -r(k))$ . Using Eq. (5) we have

$$x_{\text{inc}}^2(k) + z_{\text{inc}}^2(k) + 2r(k)z_{\text{inc}}(k) = 0 \quad (6)$$

The incremental motion in the  $x_t$ -direction ( $x_{\text{inc}}(k)$ ) is given by the following trigonometric relationship (Fig. 3b):

$$x_{\text{inc}}(k) = r(k) \sin\left(\frac{Tv_{\text{ins}}}{r(k)}\right) \quad (7)$$

where  $v_{\text{ins}}$  and  $T$  are the insertion velocity and the discrete time period of the insertion, respectively. Using Eqs. (6) and (7), the incremental needle tip motion ( $\hat{\mathbf{p}}_{\text{inc}}^t(k)$ ) in the needle tip frame ( $\mathcal{H}_t$ ) is written as

$$\hat{\mathbf{p}}_{\text{inc}}^t(k) = \begin{bmatrix} x_{\text{inc}} \\ y_{\text{inc}} \\ z_{\text{inc}} \end{bmatrix} = \begin{bmatrix} r(t) \sin\left(\frac{Tv_{\text{ins}}}{r(k)}\right) \\ 0 \\ r(k) - \sqrt{r^2(k) - x_{\text{inc}}^2(k)} \end{bmatrix} \quad (8)$$

The incremental tip motion is transformed from the tip frame ( $\mathcal{H}_t$ ) to the reference frame ( $\mathcal{H}_0$ ) using a rotation matrix  $\mathbf{R}(k)$  (Fig. 3b). The rotation matrix ( $\mathbf{R}(k)$ ) is given by  $\mathbf{R}(k) = \mathbf{R}_{\text{tip}}(k)\mathbf{R}_{\alpha}(k)$ , where  $\mathbf{R}_{\alpha}(k)$  is a rotation matrix around the  $x_t$ -axis of the needle tip frame by the rotation angle defined by the steering algorithm ( $\alpha(k)$ ) and  $\mathbf{R}_{\text{tip}}(k)$  is the current needle tip orientation estimated by the US-based tracking system. Thus, using Eq. (8), the needle tip position predicted by the deflection model is written as

$$\hat{\mathbf{p}}_{\text{tip}}^0(k+1) = \hat{\mathbf{p}}_{\text{tip}}^0(k) + \mathbf{R}(k)\hat{\mathbf{p}}_{\text{inc}}^t(k) \quad (9)$$

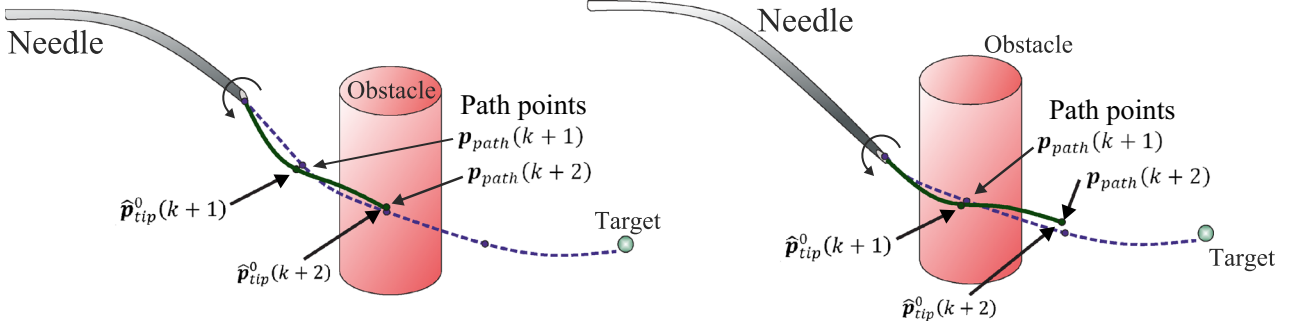


**FIGURE 4.** The steering algorithm computes the best sequence of rotations to be applied on the instant  $k$  and  $k + 1$  that minimize the path tracking error, where  $k$  is the discrete index. The path tracking error is defined as  $(\hat{\mathbf{p}}_{\text{tip}}^0(k+1) - \mathbf{p}_{\text{path}}^0(k+1)) + (\hat{\mathbf{p}}_{\text{tip}}^0(k+2) - \mathbf{p}_{\text{path}}^0(k+2))$ , where  $\hat{\mathbf{p}}_{\text{tip}}^0$  is the predicted needle tip position and  $\mathbf{p}_{\text{path}}^0$  is the path point. The needle deflection model is used to predict the needle tip position at the subsequent steps. The rotation computed for the instant  $k$  is performed and in the next instant a new pair of rotations is computed.

This needle deflection model is used in the steering algorithm to predict the needle tip motion and define the best rotation that has to be applied.

### Steering Algorithm

The steering algorithm defines the needle rotation to be performed about the insertion axis. The rotations orient the needle to follow the desired path and to reach the target. The needle rotation can be calculated by aligning the current tip pose towards the next point on the desired path. However, when the needle steering algorithm only takes into account the next path point, the needle might arrive the path point with a tip pose that makes the subsequent path point unreachable. This problem can be solved implementing a steering algorithm that always looks to two path points ahead.

We propose a steering algorithm that computes the best rotations to minimize the path tracking error in the next two path points (Fig. 4). This computation uses an optimization technique and the deflection model to predict the needle tip motion. The optimization algorithm based on the golden search method is implemented to minimize the function:

$$J(k) = \left\| \hat{\mathbf{p}}_{\text{tip}}^0(k+1) - \mathbf{p}_{\text{path}}^0(k+1) + \hat{\mathbf{p}}_{\text{tip}}^0(k+2) - \mathbf{p}_{\text{path}}^0(k+2) \right\| \quad (10)$$

where  $\mathbf{p}_{\text{path}}$  is the desired path point. The steering algorithm computes the best rotations to be applied at the current step ( $k$ ) and at the next step ( $k + 1$ ), however only the rotation at the step ( $k$ ) is applied. At step  $k + 1$  a new pair of rotations are computed. The algorithm is executed every 1.2 s. This period is enough to compute the rotation and to perform the curvature estimation without compromising the steering accuracy.<sup>19</sup> Moreover, this period allows us to perform the same online curvature estimation technique presented and evaluated by Moreira *et al.*<sup>19</sup>

### Curvature Estimation

The needle deflection may vary during the needle insertion. This variation occurs when the needle penetrates different tissue layers and due to the tissue inhomogeneity. The curvature estimation is performed to update the needle deflection model used in the steering algorithm. The technique combines the biomechanics-based curvature estimation presented in the previous subsection and online curvature estimation.

The online curvature estimation uses blocks of needle tip poses to perform a least square curve fitting. Each block is composed by the last 30 needle tip poses estimated by the US-based needle tracking.<sup>19</sup> The curvature estimation is synchronized with the steering algorithm to assure that in one block of needle tip pose data, the needle is not rotated. Thus, the needle performs a planar circular motion in the  $xz_t$ -plane during this period of time. The online estimation is performed with the same frequency of the steering algorithm, i.e., every 1.2 s.

The online curvature estimation uses a principal component analysis (PCA) algorithm to find the plane where the deflection path is performed.<sup>19</sup> The 2D projected data is then applied in a least square algorithm to find the radius of curvature. However, when the needle path is similar to a straight line, i.e., the needle is penetrating a soft tissue, the least square solution might not be guaranteed. In order to improve the robustness of the curvature estimation, the online estimation is fused with the biomechanics-based curvature estimation.

The data fusion is performed using an indirect feed forward Kalman filter. The system diagram is presented Fig. 5. The Kalman filter is used to filter and estimate the error between the online and the offline estimations. This error between the two estimations is modeled as a random walking process, and the Kalman states are the estimation error and its first derivative. The indirect Kalman filter is experimentally

tuned with system noise covariance of 0.01 and measurement noise covariance of 0.1. The curvature estimation and the steering algorithm are then evaluated under experiments in inhomogeneous tissues.

## RESULTS

In this section, we present the experimental setup used to steer the flexible needle into gelatin phantoms and biological tissues, the experimental cases, and the final steering results.

### Experimental Setup

The experimental setup, composed of the needle insertion device and the US-based needle tracking system, is shown in Fig. 1. The needle insertion device has two degrees of freedom: translation along and rotation about the insertion axis.<sup>1</sup> The needle used in the experiments is made of Nitinol ( $E = 75$  GPa). It is a solid wire with diameter of 0.5 mm and has a bevel tip angle of 30°. The US-based needle tracking system uses a 18 MHz high definition US transducer (Transducer 18L6HD, Siemens ACUSON S2000 US system, Siemens AG, Erlangen, Germany) to estimate the needle tip pose. The ARFI imaging technique is performed using the same US system and the Young's modulus of each phantom is estimated as described in the “Materials and methods” section.

### Experimental Cases

Three experimental cases are used to evaluate the needle steering algorithm, the needle tracking and the curvature estimation. Phantoms are prepared for each experimental case. A gelatin phantom and a biological phantom are presented in Fig. 6. The experimental cases are:

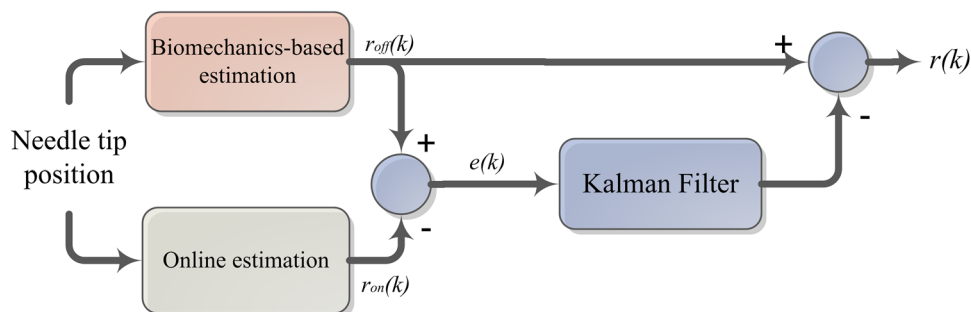


**FIGURE 5.** The indirect Kalman filter used to fuse the offline estimated radius of curvature ( $r_{off}(k)$ ) and the online estimated radius curvature ( $r_{on}(k)$ ). The Kalman filter is used to filter the estimation error between the online and the offline estimations ( $e(k)$ ), which is used to correct the final radius of curvature ( $r(k)$ ).

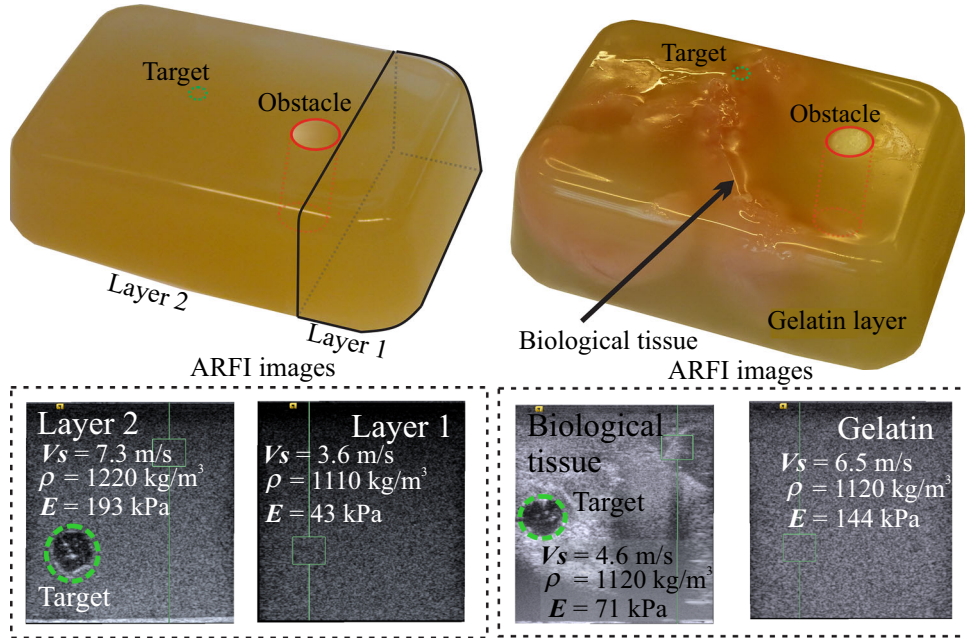


**FIGURE 6.** Representative figures of gelatin and biological phantoms used in the experiments. The phantom on the left has two layers with different gelatin concentrations, a real obstacle and a real target are embedded inside the phantom. The phantom on the right is composed of gelatin and biological tissue (*ex vivo* chicken breast tissue) and a real obstacle is embedded inside the phantom. For Case 2 a real target is also embedded in the phantom, while in Case 3 a virtual moving target is used. The ultrasound-based acoustic radiation force impulse (ARFI) imaging technique is used to calculate the Young's modulus ( $E$ ) of each layer of the phantom by estimating the shear wave velocity ( $V_s$ ).

- Case 1—Two layer phantom: The needle is steered towards a real target in a two-layer phantom while avoiding an real obstacle.
- Case 2—Biological phantom: The needle is steered towards a real target inside an biological tissue (*ex vivo* chicken breast) embedded in a gelatin phantom while avoiding an real obstacle.
- Case 3—Biological phantom with moving target: The needle is steered towards a moving virtual target inside an biological tissue (*ex vivo* chicken breast) embedded in a gelatin phantom while avoiding an obstacle. The target movement is a sinusoidal motion to represent disturbances that might be caused by physiological processes.

The ARFI imaging technique is used to estimate Young's modulus of each phantom layer. The first layer of the two-layer phantom (Case 1) is prepared with 90% water, 9% gelatin, and 1% silica, which results in  $E \sim 25$  kPa. The second layer has 80% water, 19% gelatin, 1% silica and  $E \sim 90$  kPa. The silica powder is added to all gelatin to simulate the acoustic scattering of human tissue in ultrasound images. The two-layer phantom has elasticity similar to a normal fat tissue ( $E \sim 22$  kPa) and a cancerous prostate ( $E \sim 96$  kPa).<sup>13</sup> The phantoms for Case 2 and Case 3

are prepared embedding a chicken breast tissue in gelatin prepared with 84% water, 15% gelatin, and 1% silica. The targets of Case 1 and Case 2 are made of a mixture of 80% water, 19.5% Polyvinyl alcohol (SigmaAldrich Chemie B.V., Zwijndrecht, The Netherlands). The targets are fabricated with a radius of 3 mm, which is within the range of the prostate tumor.<sup>10</sup> We use the function defined by Eq. (4) to define the needle curvature for each phantom layer based on the Young's modulus estimated by the ARFI imaging technique. The phantoms are prepared using molds with pre-defined dimensions, which makes the position of each layer known.

Before each experiment of Case 1 and Case 2, the phantom is scanned by the US transducer to detect the obstacle and target locations. This information is used to calculate the desired needle path in order to reach the target while avoiding the obstacle. In Case 3 only the obstacle location is detected. The path is defined based on the obstacle location and the initial position of the virtual target.

### Experimental Results

Five needle insertions are performed for each experimental case. The needle is inserted with a constant velocity of 1 mm/s. The insertion stops when the

tracked needle tip position and the target positions in the  $x$ -axis are the same. In Case 3 the target motion is defined by  $x_{tar} = 85.0 + 2.0 \sin(\pi t)$ , where  $x_{tar}$  is the target location in the  $x$ -axis and  $t$  is the time in seconds. The target motion with a frequency of 0.5 Hz is applied to represent a disturbance caused by respiration.

The average of targeting error and the standard deviation in five experiments of Case 1 is  $0.42 \pm 0.17$  mm. In biological tissue, Case 2 has an average of targeting error of  $1.56 \pm 0.52$  mm, while in Case 3 the average of targeting error is  $1.63 \pm 0.29$  mm. The targeting error is calculated as the Euclidian distance between the final needle tip position and the center of the target. The targeting errors for the three cases are in the range of the smallest tumor that can be detected by US images (2 mm). The results of Case 3 show that, even with target motion in biological tissue, the system is able to achieve a targeting error of 1.63 mm. One representative experimental result for each case is shown in Fig. 7. In Case 1, the needle crosses the layer interface at an insertion depth of 22 mm. In Case 2 and Case 3 the position of the layer interface varies due to the irregular shape of the biological tissue and occurs between 20 and 30 mm, depending on the phantom. The evolution of the estimated radius of curvature is presented in Fig. 8. It is also possible to notice that the curvature stabilizes with a value different from the one estimated using the biomechanics-based offline estimation. This difference happens because the elastic properties of the gelatin phantom might vary accord-

ing to its temperature.<sup>1</sup> In Case 2 and Case 3 the variation of the curvature is more pronounced when the needle is inside the biological tissue due to the inhomogeneity of the tissue. The results of needle curvature estimation demonstrate the importance of combining the biomechanics-based offline estimation with the online estimation.

## DISCUSSION

This study presents a novel flexible needle steering method combining optimal rotation control, biomechanics-based model and online curvature estimation. The algorithm defines the best needle rotations that minimize the path tracking error, hence minimizing the targeting error. The curvature estimation is used to update the steering algorithm in real time during the insertion. Experiments are performed to evaluate the targeting accuracy and the curvature estimation of the proposed needle steering method. The average targeting errors ranges between  $0.42 \pm 0.17$  and  $1.63 \pm 0.29$  mm. During experiments in biological tissues (Case 2 and Case 3), the needle tracking is affected by the artifacts present in the US image of the *in vitro* biological tissue. Recently, similar experiments were performed by Patil *et al.*<sup>22</sup> in biological tissues with an average error ranging from  $2.38 \pm 1.02$  to  $3.60 \pm 1.85$  mm. Although the experimental conditions are not the same, it is interesting to notice that the targeting errors achieved by Patil *et al.*<sup>22</sup> are significant higher than the errors presented in this study.

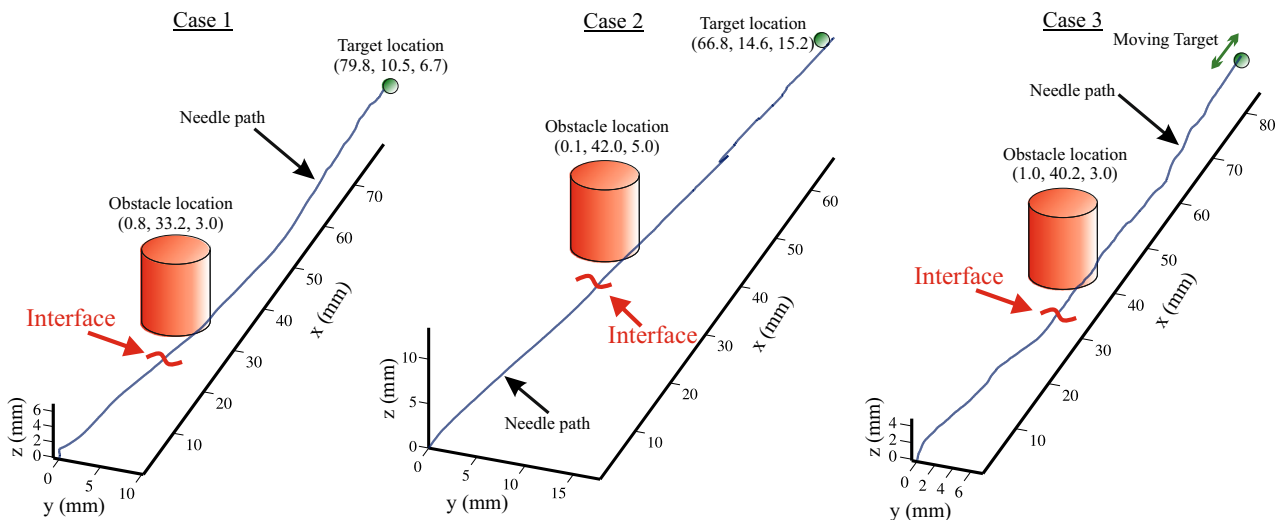


**FIGURE 7.** Representative experimental result for each experimental case. In Case 1 the bevel-tipped flexible needle is steered towards a real target while avoiding a real obstacle in a two-layer gelatin phantom. In Case 2, the needle is steered towards a real target while avoiding a real obstacle in a biological phantom. Moreover, in Case 3 the needle is steered the needle is steered towards a virtual moving target while avoiding a real obstacle in a biological phantom. Please refer to the accompanying video that demonstrates the experimental results.

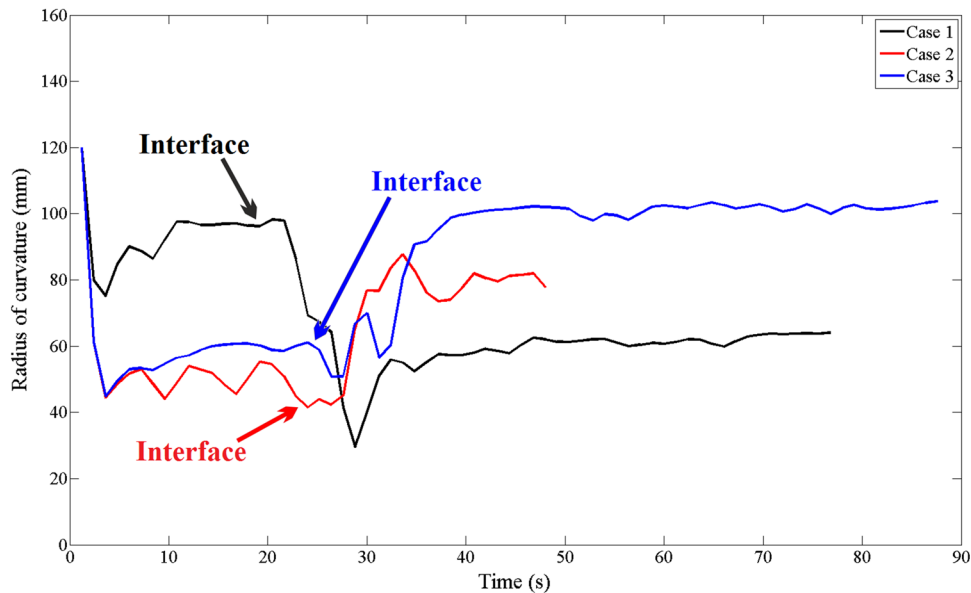


**FIGURE 8.** Estimated maximum curvature combining biomechanics-model and online curvature estimation during the needle steering experiments. The black line is the curvature estimation in the gelatin phantom (Case 1), the red and blue line are the curvature estimation in the biological phantom composed of gelatin and *ex vivo* chicken breast tissue (Case 2 and 3, respectively). The radius of curvatures estimated offline by the biomechanics-based model in Case 1 are 114 mm for layer 1 and 65 mm for layer 2. In Case 2 the radius of curvatures are 70 mm for layer 1 and 97 mm for the biological tissue. In Case 3 the radius of curvatures are 68 mm for layer 1 and 92 mm for the biological tissue.

Additionally, in our previous work using only the online curvature estimation, the targeting error is also higher than the error reported in this paper, ranging between 0.98 and 2.46 mm. It is also important to highlight that in all experiments performed in this study the targeting error is below 2 mm, which is the size of the smallest lesion visible in US images.<sup>1</sup> The targeting error smaller than 2 mm and the validation of the curvature estimation algorithm is an important step towards a robot-assisted needle steering. However, there are some issues that have to be consider in order to implement the presented technique in clinical practice. Currently, the US-based needle tracking is disturbed by tissue artifacts, which can increase the tracking error. A redundant needle tracking system might be necessary to guarantee that the needle tip will be tracked during the entire procedure. Another clinical aspect is that during *in vivo* insertion, the presence of physiological process might affects the biomechanical characteristics of some tissues. In those cases, the Kalman filter used to fuse the offline and online estimation has to be carefully tuned in order to guarantee that changes in the needle curvature will be tracked by the online estimation. Moreover, the interface between the tissue layers in the human body might not be clearly definable and a pre-operative scan of the region might be needed in order to define the tissue layers. Additionally, to increase the safety of robot-assisted needle steering, the presented technique can be implemented in a human-in-the-loop steering system.<sup>21</sup>

Future work will focus on enhancing the US-based needle tracking to increase it robustness in biological tissue. We plan to integrate the needle deflection model into the tracking algorithm and to apply more advanced image processing techniques to properly detect the needle tip. We also plan use magnetic trackers and develop a needle tracking algorithm able to fuse the US-based and electromagnetic-based needle tracking. Moreover, we plan to investigate needle steering in a moving phantom. We are currently adapting the experimental setup to provide a sinusoidal motion to the phantom in the insertion axis in order replicate the breathing motion. Our study has demonstrated the feasibility and the benefits of merging online and offline curvature estimation to perform flexible needle steering in biological tissues.

## ELECTRONIC SUPPLEMENTARY MATERIAL

The online version of this article ([doi:10.1007/s10439-014-1203-5](https://doi.org/10.1007/s10439-014-1203-5)) contains supplementary material, which is available to authorized users.

## REFERENCES

- Abayazid, M., R. J. Roesthuis, R. Reilink, and S. Misra. Integrating deflection models and image feedback for real-time flexible needle steering. *IEEE Trans. Robot.* 29:542–553, 2013.

- <sup>2</sup>Abayazid, M., G. Vrooijink, S. Patil, R. Alterovitz, and S. Misra. Experimental evaluation of ultrasound-guided 3D needle steering in biological tissue. *Int. J. CARS* 9:931–939, 2014.
- <sup>3</sup>Abolhassani, N., R. Patel, and M. Moallem. Needle insertion into soft tissue: a survey. *Med. Eng. Phys.* 29:413–431, 2007.
- <sup>4</sup>Abolhassani, N. and R. V. Patel. Deflection of a flexible needle during insertion into soft tissue. In: 28th Annual International Conference of IEEE Engineering in Medicine and Biology Society (EMBS), USA, 2006, pp. 3858–3861.
- <sup>5</sup>Asadian, A., M. R. Kermani, and R. V. Patel. An analytical model for deflection of flexible needles during needle insertion. In: Intelligent Robots and Systems (IROS), 2011, pp. 2551–2556.
- <sup>6</sup>Bernardes, M. C., B. V. Adorno, P. Poignet, and G. A. Borges. Robot-assisted automatic insertion of steerable needles with closed-loop imaging feedback and intraoperative trajectory replanning. *Mechatronics* 23:630–645, 2013.
- <sup>7</sup>Chun, H. Y., M. T. Kim, H. C. Jung, K. Ko, and K. G. Kim. Experimental study on needle insertion force for breast. *World Congr. Med. Phys. Biomed. Eng.* 39:2182–2183, 2013. doi:[10.1007/978-3-642-29305-4\\_572](https://doi.org/10.1007/978-3-642-29305-4_572).
- <sup>8</sup>Cowan, N. J., K. Goldberg, G. S. Chirikjian, G. Fichtinge, R. Alterovitz, K. B. Reed, V. Kallem, W. Park, S. Misra, and A. M. Okamura. Robotic needle steering: design, modeling, planning, and image guidance. In: Surgical Robotics—Systems, Applications, and Visions, edited by J. Rosen, B. Hannaford, and R. Satava. New York: Springer, 2011, pp. 557–582.
- <sup>9</sup>DiMaio, S. P., and S. E. Salcudean. Needle insertion modeling and simulation. *IEEE Trans. Robot. Autom.* 19:864–875, 2003.
- <sup>10</sup>Eichelberger, L. E., M. O. Koch, J. K. Daggi, T. M. Ulbright, J. N. Eble, and L. Cheng. Predicting tumor volume in radical prostatectomy specimens from patients with prostate cancer. *Am. J. Clin. Pathol.* 120:386–391, 2003.
- <sup>11</sup>Engh, J., G. Podnar, D. Kondziolka, and C. Riviere. Toward effective needle steering in brain tissue. In: IEEE EMBS Annual International Conference, 2006, pp. 559–562.
- <sup>12</sup>Fung, Y. C. Biomechanics: Mechanical Properties of Living Tissue. New York: Springer, 1993.
- <sup>13</sup>Gefen, A., and B. Dilmoney. Mechanics of the normal woman's breast. *Technol. Health Care* 15:259–271, 2007.
- <sup>14</sup>Glozman, D., and M. Shoham. Image-guided robotic flexible needle steering. *IEEE Trans. Rob.* 23:459–467, 2007.
- <sup>15</sup>Majewicz, A., S. P. Marra, M. G. van Vledder, L. MingDe, M. A. Choti, D. Y. Song, and A. M. Okamura. Behavior of tip-steerable needles in ex vivo and in vivo tissue. *IEEE Trans. Biomed. Eng.* 59:2705–2715, 2012.
- <sup>16</sup>Minhas, D. S., J. A. Engh, M. M. Fenske, and C. N. Riviere. Modeling of needle steering via duty-cycled spinning. In: IEEE EMBS Annual International Conference, 2007, pp. 5432–5435.
- <sup>17</sup>Misra, S., K. T. Ramesh, and A. M. Okamura. Modeling of tool-tissue interactions for computer-based surgical simulation: a literature review. *Presence Teleop. Virt.* 17:463–491, 2008.
- <sup>18</sup>Misra, S., K. B. Reed, B. W. Schafer, K. T. Ramesh, and A. M. Okamura. Mechanics of flexible needles robotically steered through soft tissue. *Int. J. Robot. Res.* 23:1640–1660, 2010.
- <sup>19</sup>Moreira, P., S. Patil, R. Alterovitz, and S. Misra. Needle steering in biological tissue using ultrasound-based online curvature estimation. In: IEEE International Conference on Robotics Automation, 2014, pp. 4368–4373.
- <sup>20</sup>Nightingale, K., S. McAleavy, and G. Trahey. Shear-wave generation using acoustic radiation force: in vivo and ex vivo results. *Ultrasound Med. Biol.* 29:1715–1723, 2003.
- <sup>21</sup>Pacchierotti, C., M. Abayazid, S. Misra, and D. Prattichizzo. Teleoperation of steerable flexible needles by combining kinesthetic and vibratory feedback. *IEEE Trans. Haptics*, 1–1, 2014. doi:[10.1109/TOH.2014.2360185](https://doi.org/10.1109/TOH.2014.2360185).
- <sup>22</sup>Patil, S., J. Burgner, R. J. Webster, and R. Alterovitz. Needle steering in 3-D via rapid replanning. *IEEE Trans. Robot.* 30:853–864, 2014. doi:[10.1109/TRO.2014.2307633](https://doi.org/10.1109/TRO.2014.2307633).
- <sup>23</sup>Podder, T. K., D. P. Clark, J. Sherman, D. Fuller, E. M. Messing, D. J. Rubens, J. G. Strang, Y. D. Zhang, W. O'Dell, W. S. Ng, and Y. Yu. Effects of tip geometry of surgical needles: an assessment of force and deflection. In: European Medical and Biological Engineering Conference (EMBEC), 2005.
- <sup>24</sup>Robert, A. L. G., G. Chagnon, I. Bricault, P. Cinquin, and A. Moreau-Gaudry. A generic three-dimensional static force distribution basis for a medical needle inserted into soft tissue. *J. Mech. Behav. Biomed. Mater.* 28:156–170, 2013.
- <sup>25</sup>Roesthuis, R. J., M. Kemp, J. J. van den Dobbelen, and S. Misra. Three-dimensional needle shape reconstruction using an array of fiber bragg grating sensors. *IEEE/ASME Trans. Mechatron.* 19:1115–1126, 2014.
- <sup>26</sup>Sadjadi, H., K. Hashtrudi-Zaad, and G. Fichtinger. Fusion of electromagnetic trackers to improve needle deflection estimation: simulation study. *IEEE Trans. Biomed. Eng.* 60:2706–2715, 2013. doi:[10.1109/TBME.2013.226258](https://doi.org/10.1109/TBME.2013.226258).
- <sup>27</sup>van Veen, Y. R. J., A. Jahya, and S. Misra. Macroscopic and microscopic observations of needle insertion into gels. *Proc. Inst. Mech. Eng. [H]* 226:441–449, 2012.
- <sup>28</sup>Vrooijink, G. J., M. Abayazid, S. Patil, R. Alterovitz, and S. Misra. Needle path planning and steering in a three-dimensional non-static environment using two-dimensional ultrasound images. *Int. J. Robot. Res.* 33:1361–1374, 2014.
- <sup>29</sup>Webster, III, R. J., J. S. Kim, N. J. Cowan, G. S. Chirikjian, and A. M. Okamura. Nonholonomic modeling of needle steering. *Int. J. Robot. Res.* 25:509–525, 2006.
- <sup>30</sup>Yaniv, Z., P. Cheng, E. Wilson, T. Popa, D. Lindisch, E. Campos-Nanez, H. Abeledo, V. Watson, K. Cleary, and F. Banovac. Needle-based interventions with the image-guided surgery toolkit (IGSTK): from phantoms to clinical trials. *IEEE Trans. Biomed. Eng.* 57:922–933, 2010.